Experimental and Computational Multiphase Flow
Vol. 5, No. 2, 2023, 178–191
https://doi.org/10.1007/s42757-021-0130-6

Numerical investigation of particle motion at the steel–slag interface in continuous casting using VOF method and dynamic overset grids

Xiaomeng Zhang[1,2] (✉), Stefan Pirker[2], Mahdi Saeedipour[2]

1. K1-MET GmbH, Stahlstrasse 14, 4020 Linz, Austria
2. Department of Particulate Flow Modelling, Johannes Kepler University, 4040 Linz, Austria

Abstract

The capillary interactions are prominent for a micro-sized particle at the steel–slag interface. In this study, the dynamics of a spherical particle interacting with the steel–slag interface is numerically investigated using the volume of fluid method in combination with the overset grid technique to account for particle motion. The simulations have shown the particle's separation process at the interface and successfully captured the formation and continuous evolution of a meniscus in the course of particle motion. A sensitivity analysis on the effect of different physical parameters in the steel–slag–particle system is also conducted. The result indicates that the wettability of particle with the slag phase is the main factor affecting particle separation behavior (trapped at the interface or fully separated into slag). Higher interfacial tension of fluid interface and smaller particle size can speed up the particle motion but have less effect on the equilibrium position for particle staying at the interface. In comparison, particle density shows a minor influence when the motion is dominated by the capillary effect. By taking account of the effect of meniscus and capillary forces on a particle, this study provides a more accurate simulation of particle motion in the vicinity of the steel–slag interface and enables further investigation of more complex situations.

Keywords

inclusion removal
steel–slag interface
capillary interaction
wettability
volume of fluid (VOF) method
overset grid

Article History

Received: 25 June 2021
Revised: 20 November 2021
Accepted: 15 December 2021

Research Article

1 Introduction

With the ever-increasing requirements for high-quality steel products, steel cleanliness is becoming increasingly demanding. The cleanliness largely depends on the control of non-metallic inclusions (NMIs) which are an inevitable component present in molten steel. They generate as deoxidation products and may also come from other sources such as refectory erosion during processing and could cause many defects in the steel product (Zhang and Thomas, 2003). One common control strategy for NMIs is to remove them from the liquid steel to the top-covering slag. Significant efforts have been made to characterize and optimize the bulk flow conditions, with varying degrees of success in facilitating the removal of inclusions (Miki and Thomas, 1999; Zhang et al., 2000; Thomas and Zhang, 2001). However, the removal efficiency tends to be overestimated because these studies usually assume that inclusions are naturally absorbed by slag as long as they reach the interface. Actually, in addition to the transport of inclusion in molten steel, the separation of inclusion at the steel–slag interface and the following dissolution in the slag are two integral parts for inclusion removal (Sridhar and Cramb, 2000; Park et al., 2006; Reis et al., 2014; Michelic et al., 2016). Particularly, as the critical intermediate step, the separation process interacts closely with the other two steps and greatly affects the removal efficiency of inclusion. Inclusion's separation behavior (trapped at the interface or completely entering into slag) will influence the subsequent dissolution kinetics. A limited dissolution reaction may happen due to insufficient contact with the slag for inclusions that cannot be separated entirely. In turn, trapped inclusions or inclusions that rest near the interface without a fast dissolution can also be detrimental to further

✉ xiaomeng.zhang@jku.at

Nomenclature

Bo	Bond number
D	particle diameter (m)
$\boldsymbol{F}_\sigma$	capillary force (N)
g	gravity constant (m/s^2)
$\boldsymbol{I}$	moment of inertia tensor (kg·m^2)
k	interfacial curvature (m^{-1})
m	particle mass (kg)
$\boldsymbol{M}$	angular momentum vector (kg·m^2/s)
$\hat{\boldsymbol{n}}$	unit normal vector
p	pressure (Pa)
R	particle radius (m)
$\boldsymbol{R}$	transformation matrix
Re	Reynolds number
t	time (s)
$\hat{\boldsymbol{t}}$	unit tangent vector
$\boldsymbol{u}$	linear velocity vector of particle (m/s)
U	terminal velocity of particle (m/s)
$\boldsymbol{U}$	velocity vector of mixture of fluids (m/s)
Z	vertical coordinate (m)

Greek symbols

α	volume fraction of fluid
δ	Dirac delta function
θ	three-phase contact angle (°)
μ	dynamic viscosity (Pa·s)
ρ	material density (kg/m^3)
σ	interfacial tension coefficient (N/m)
$\boldsymbol{\tau}$	viscous stress tensor (Pa)
$\boldsymbol{\omega}$	angular velocity vector of particle (rad/s)

Subscripts

b	body coordinate system
i	inertial frame of reference
I	inclusion particle
M	metal
S	slag
w	particle surface

separation (Sridhar and Cramb, 2000). In these situations, inclusions have the risk of being brought back and once again contaminating the molten steel (Bouris and Bergeles, 1998; Sridhar and Cramb, 2000; Choi and Lee, 2003). Some experiments were conducted for in-situ observations. However, it turned out that a detailed separation process, especially for a solid inclusion, was hard to observe because it happened in a very short time, and only the relatively long-lasting agglomeration of inclusions at the interface could be seen (Lee et al., 2001; Mu et al., 2018).

Numerical approaches have shown great promise in revealing the process of the interfacial separation of inclusion. Existing studies are mostly based on the mathematical model developed by Nakajima and Okamura (1992). According to the particle Reynolds number $Re_\mathrm{I} = \rho_\mathrm{M} U D_\mathrm{I}/\mu_\mathrm{M}$ (terminal velocity of particle $U = (1/18) D_\mathrm{I}^2 (\rho_\mathrm{M} - \rho_\mathrm{I}) g/\mu_\mathrm{M}$, particle diameter and density D_I and ρ_I, steel density and dynamic viscosity ρ_M and μ_M, respectively), two scenarios are proposed in this model—a steel film existing ahead of a particle ($Re_\mathrm{I} \geq 1$) or without such film ($Re_\mathrm{I} < 1$) before the particle first contacts with the interface. Only the latter is relevant to particles in the production as most of them are relatively small and will not or can only cause a negligible liquid film. In this case, the particle reaches the horizontal steel–slag interface in terminal velocity, and the interface remains flat during the whole separation process. Particle either passing through or staying at the interface is determined according to its displacement. Strandh et al. (2005a, 2005b) applied this model to investigate the separation of solid inclusions in tundish conditions and the separation of liquid inclusions by introducing the inclusion viscosity. They have pointed out that the essential parameters on the inclusion transfer are the interfacial tensions and the slag viscosity. Bouris and Bergeles (1998) also used Nakajima's model to further investigate the possibility of re-entrainment back into the steel for particles that reach an equilibrium state at the interface partially immersed in the molten steel by considering the lift forces acting on a particle arising from the turbulent boundary near the steel–slag interface. Besides, based on Nakajima's model, Liu et al. (2016) considered the effect of different Re numbers of fluid on the drag force acting on the particle. Although improvements have been made, the above studies still did not account for the effect of the meniscus during separation. However, it is considered as a fundamental phenomenon in such a multiphase flow regime, i.e., interactions between a small particle with a stratified interface, and relevant studies have been conducted in many other fields (Aveyard et al., 2000; Schellenberger et al., 2018; Tang and Cheng, 2018). These studies indicate a strong connection between particle removal from a liquid surface and the meniscus shape, but it is still challenging to correlate force and shape directly. For the steel–slag system, which is characterized by a large interfacial tension at the interface, the capillary action with a micro-sized inclusion particle should be noteworthy. Neglecting interfacial deformation is expected to lead to inaccurate estimation of inclusion motion at the steel–slag interface, and the influence of meniscus shape changing on the motion of

non-spherical inclusions might be particularly important (Shannon and Sridhar, 2005).

The present work directly displays the dynamic motion of a spherical particle at the steel–slag interface through a moving-grid technique. The formation of the meniscus and its continuous evolution due to three-phase interactions are captured. A more accurate estimation of resulting capillary force and particle motion at the interface is obtained. A sensitivity analysis on the effect of different physical parameters in the steel–slag–particle system is also conducted. The current study provides an understanding of the fundamental aspects of inclusion separation at the steel–slag interface. This simulation approach can be further developed to incorporate more physical mechanisms involved in industrial situations. Future work will focus on the refinement of the model on interfacial separation and the connection to the macroscopic bulk flow to optimize the inclusion removal process.

2 Numerical model

2.1 Governing equations

The molten steel and slag are considered as two incompressible and immiscible fluids. In the course of particle motion, the meniscus (deformation of steel–slag interface) is tracked by employing the volume of fluid (VOF) method (Hirt and Nichols, 1981), which is implemented by solving the continuity equation and the momentum equation together with the volume fraction function. The governing equations involved are as Eqs. (1)–(3):

$$\nabla \cdot \boldsymbol{U} = 0 \tag{1}$$

$$\frac{\partial(\rho \boldsymbol{U})}{\partial t} + \nabla \cdot (\rho \boldsymbol{U}\boldsymbol{U}) = -\nabla p + \nabla \cdot \boldsymbol{\tau} + \rho \boldsymbol{g} + \boldsymbol{F}_\sigma \tag{2}$$

$$\frac{\partial \alpha}{\partial t} + \nabla \cdot (\alpha \boldsymbol{U}) = 0 \tag{3}$$

In the above equations, $\boldsymbol{U}$ is the velocity vector of the mixture of fluids, p is the pressure, $\boldsymbol{g}$ is the vector of gravitation, and $\boldsymbol{\tau}$ is the viscous stress tensor with the form of $\mu(\nabla \boldsymbol{U} + \nabla \boldsymbol{U}^{\mathrm{T}})$ for Newtonian fluids. The scalar function α denotes the volume fraction field which determines the phase averaged properties ρ and μ as Eqs. (4) and (5):

$$\rho = \alpha \rho_{\mathrm{S}} + (1-\alpha)\rho_{\mathrm{M}} \tag{4}$$

$$\mu = \alpha \mu_{\mathrm{S}} + (1-\alpha)\mu_{\mathrm{M}} \tag{5}$$

where subscripts M and S refer to the steel and the slag phases, respectively.

In Eq. (2), the surface tension force $\boldsymbol{F}_\sigma$ is calculated by the continuum surface force (CSF) method (Brackbill et al., 1992) and reads

$$\boldsymbol{F}_\sigma = \sigma k \hat{\boldsymbol{n}} \delta \tag{6}$$

where σ is the surface tension coefficient, and δ is the delta function that restricts the capillary force to the interface. k and $\hat{\boldsymbol{n}}$ are the interfacial curvature and the unit normal vector to the interface, respectively, which are computed based on the gradient of phase volume fraction and written as

$$\hat{\boldsymbol{n}} = \frac{\nabla \alpha}{|\nabla \alpha|} \tag{7}$$

$$k = -\nabla \cdot \hat{\boldsymbol{n}} \tag{8}$$

Specifically, at cells adjacent to the particle surface, the unit normal vector to the interface is adjusted by solid surface wettability, which is determined by the contact angle θ between the fluid interface and the particle surface:

$$\hat{\boldsymbol{n}} = \hat{\boldsymbol{n}}_{\mathrm{w}} \cos\theta + \hat{\boldsymbol{t}}_{\mathrm{w}} \sin\theta \tag{9}$$

where $\hat{\boldsymbol{n}}_{\mathrm{w}}$ and $\hat{\boldsymbol{t}}_{\mathrm{w}}$ are the unit vectors normal and tangential to the wall, respectively. The combination of this contact angle with the normally calculated surface normal one cell away from the wall determines the local curvature of the interface.

Once the fluid field is obtained by solving the equations above, the resulting flow forces acting on the solid particle are treated as the pressure and the viscous components in Fluent and calculated by numerical integrating them over the body surface. For the motion of a rigid particle, the six degrees of freedom (6-DOF) solver is applied. The particle's translational and angular accelerations are computed using the inertial frame of reference (subscripted "i") and the body coordinate system (subscripted "b"), respectively. The governing equations which are based on Newton's second law are given by

$$m\frac{\mathrm{d}\boldsymbol{u}_{\mathrm{i}}}{\mathrm{d}t} = \sum \boldsymbol{F}_{\mathrm{i}} \tag{10}$$

$$\boldsymbol{I}_{\mathrm{b}}\frac{\mathrm{d}\boldsymbol{\omega}_{\mathrm{b}}}{\mathrm{d}t} = -\boldsymbol{\omega}_{\mathrm{b}} \times \boldsymbol{I}_{\mathrm{b}}\boldsymbol{\omega}_{\mathrm{b}} + \sum \boldsymbol{M}_{\mathrm{b}} \tag{11}$$

where m is the mass of the particle, $\boldsymbol{u}_{\mathrm{i}}$ is the linear velocity vector of the center of mass, and $\sum \boldsymbol{F}_{\mathrm{i}}$ is the sum of all forces on the rigid particle in which the gravity, the buoyancy force, the capillary force, and the drag force as well as the added-mass force are considered. For the angular motion equation, $\boldsymbol{I}_{\mathrm{b}}$ refers to the moment of inertia, the vector $\boldsymbol{\omega}_{\mathrm{b}}$ is the angular velocity of the particle about its center of mass, and $\boldsymbol{M}_{\mathrm{b}}$ is the angular momentum. The momentum and the angular velocity in different coordinates are interconverted by a transformation matrix $\boldsymbol{R}$ (Snyder et al., 2003):

$$\boldsymbol{M}_{\mathrm{b}} = \boldsymbol{R}\boldsymbol{M}_{\mathrm{i}} \tag{12}$$

$$\boldsymbol{\omega}_{\mathrm{i}} = \boldsymbol{R}^{\mathrm{T}}\boldsymbol{\omega}_{\mathrm{b}} \tag{13}$$

By solving the equations of motion, the position of the particle-attached mesh is updated, followed by calculating the volume fraction distribution and flow field for the further time step. The VOF model and the 6-DOF solver implemented in the commercial software ANSYS Fluent are employed. Further details will be discussed later.

2.2 Simulation setup and case description

In order to study the process of particle separation at the steel–slag interface, a large cuboid fluid domain including a small spherical particle with a diameter of D inside is created. As shown in Fig. 1(a), the particle is placed in the central lower position where its center (Z = 0) is two particle diameters above the bottom wall. Larger upper and surrounding spaces are reserved to avoid walls' influence on the flow and particle motion. To enable the dynamic motion of a particle and meanwhile ensure high resolution at the steel–slag interface, the computational grid is built up based on a moving-grid technique—the overset grid system in here, and discretized by purely quadrilateral grid cells. The complete grid consists of two parts—a background grid representing the fluids and a separate component grid around the particle (see Fig. 1(b)). It can be observed from the X = 0 plane (Fig. 1(c)) that these two parts simply overlap each other at first and automatically establish connectivity by interpolating cell data in the minimized overlapping region when the flow is initialized.

The separation process will start with a particle just in contact with the horizontal steel–slag interface ($Z = R$) with zero initial velocity. This is an essential initial assumption for current simulations, and its rationality will be justified in Section 2.3. A laminar flow is assumed in the vicinity of the steel–slag interface. Besides, particle surface is regarded as an ideal surface. Particle dissolution and changes in the interfacial tension of the steel–slag interface will not be considered in this paper. For the numerical method, the pressure-based coupled solver is used along with first-order schemes in temporal and momentum spatial discretization. The least squares method is employed for the overset interface interpolation. The PRESTO! scheme is used for pressure interpolation. For better VOF calculations, the least squares cell-based method and the geometric reconstruction discretization scheme are chosen for the gradients and the steel–slag interface calculating. Due to the micron-sized mesh grids, very small time steps in the order of 10^{-8} s are applied. The calculation is considered to be converged within each time step when the residuals decrease below 10^{-4}. Relevant values for two fluids and the interfacial property come from the literature (Xuan et al., 2019) and are listed in Table 1. For the steel–slag system, a reference simulation is performed initially. Then, a number of simulations are conducted for parameter studies. Particle properties for the reference case and parameter study simulations are presented in Table 2. When the effect of

Table 1 Properties of the molten phases

	Density ρ (kg/m^3)	Viscosity μ (Pa·s)	Interfacial tension σ_{MS} (N/m)
Steel (M)	7000	0.005	1.4
Slag (S)	2500	0.05	

Table 2 Properties of solid particle and content of parameter studies

	Reference case	Parameter study
Particle density ρ_I (kg/m^3)	2700	2000, 2500
Particle diameter D_I (μm)	50	25, 100
θ_{IMS} (°)	90	20, 40, 60, 120
σ_{MS} (N/m)	1.4	0.7, 0.14, 0

*$\cos\theta_{IMS} = (\sigma_{IM} - \sigma_{IS})/\sigma_{MS}$

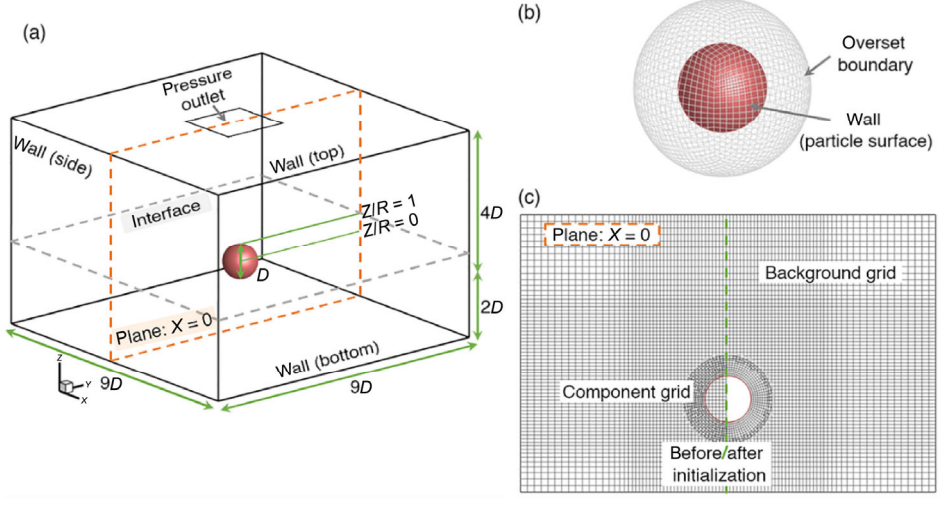

Fig. 1 (a) Schematic description of the computational domain; (b) overset component grid; and (c) complete grid at X = 0 plane.

other parameters is studied, a three-phase contact angle θ_{IMS} of 45° is chosen, which is in the typical range for solid particles in steel–slag–particle systems (Nakajima and Okamura, 1992). All of the simulations are performed with ANSYS Fluent.

2.3 Determination of initial condition

As described in Section 1, inclusion impact Reynolds number (Re_I) is a key parameter in existing models. Two situations are assumed according to Re_I: for $Re_I \geq 1$, a steel film forms ahead of the particle, while for $Re_I < 1$, the particle directly touches the steel–slag interface with its terminal velocity (Nakajima and Okamura, 1992; Strandh et al., 2005a). According to the equation of particle Reynolds number, this assumption is only relevant to the properties of the particle and the melt, which ignores the influence of interfacial tension on the movement of the particle. It is questionable that this high-temperature interface with a very high energy situation would not make a difference. To evaluate this issue, the response of the steel–slag interface to an approaching particle is analyzed by the immersed boundary method (IBM) (Lin, 2007). The fixed-grid technique constructed on simple Cartesian coordinates is used to handle moving particles, and virtual forces are introduced to represent the body's reaction to its ambient flow.

As shown in Fig. 2, a two-dimensional domain spans X = [−250, 250] μm and Y = [−400, 250] μm and is filled with immiscible molten steel and slag. The metal–slag interface is at Y = 0, and the gray region represents a moving particle with a diameter of 100 μm. The particle moves upwards in its terminal velocity (about 0.003 m/s (Odenthal et al., 2010)), and a monitoring point at the center of the interface is set to obtain the level response due to the approaching particle. Figure 3 shows the fluctuation of the interface at the monitoring point under different interfacial tensions. When there is no interfacial tension, the interface deforms easily, and the deformation is getting larger as the particle moves upwards. In comparison, interfaces with 0.14 and 1.4 N/m interfacial tension can barely see deformations, as represented by the yellow curve and the blue curve, respectively. For the cases with $\sigma_{MS} \neq 0$, the interface has slight deformations because of the effect of particle approaching, but this deformation will be stabilized by the interfacial tension. Besides, the higher interfacial tension tends to stabilize the deformation in a faster rate as shown in Fig. 3 (inserted figure). Figure 4 presents the velocity vectors in the vicinity of the approaching particle and the steel–slag interface in two cases (σ_{MS} = 0 and 1.4 N/m). It is observed that fluids between the particle and the interface discharge to both sides much faster under the effect of interface with much higher interfacial tension. Consequently, the entire interface remains almost flat in this case, while the whole interface shows distinct deformation in another situation.

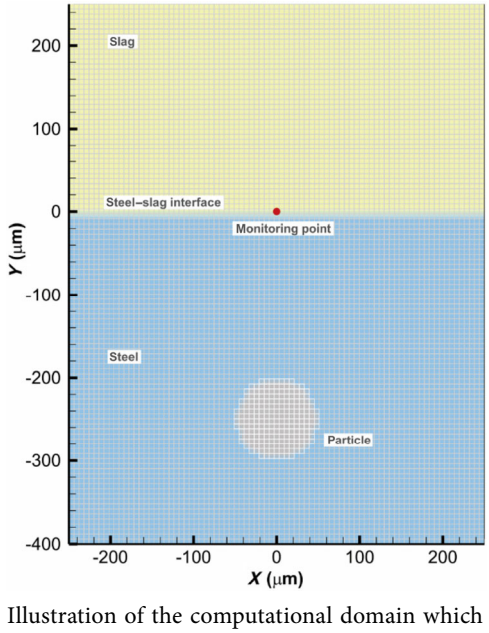

Fig. 2 Illustration of the computational domain which is composed of solid (particle) and fluid (steel and slag phases) subdomains in immersed boundary method.

Since (i) the high-temperature metal–slag interface has a very high interfacial tension (normally greater than 1 N/m), and (ii) the particle moves towards the interface with a gradually decreasing velocity which is less than its terminal velocity due to the effect of a confined drag field (Shannon et al., 2008), the particle makes no wave or disturbance upon the first contact to the interface. In other words, the influence of particle motion history on the following interfacial behavior is insignificant. Thus, starting the simulation with a particle initially touching the flat interface is believed to be a reasonable initial condition for simulation.

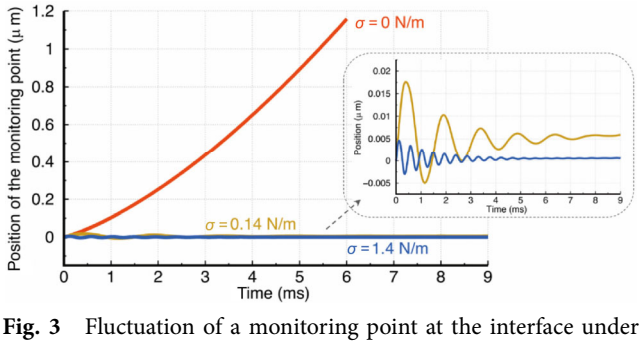

Fig. 3 Fluctuation of a monitoring point at the interface under different interfacial tensions.

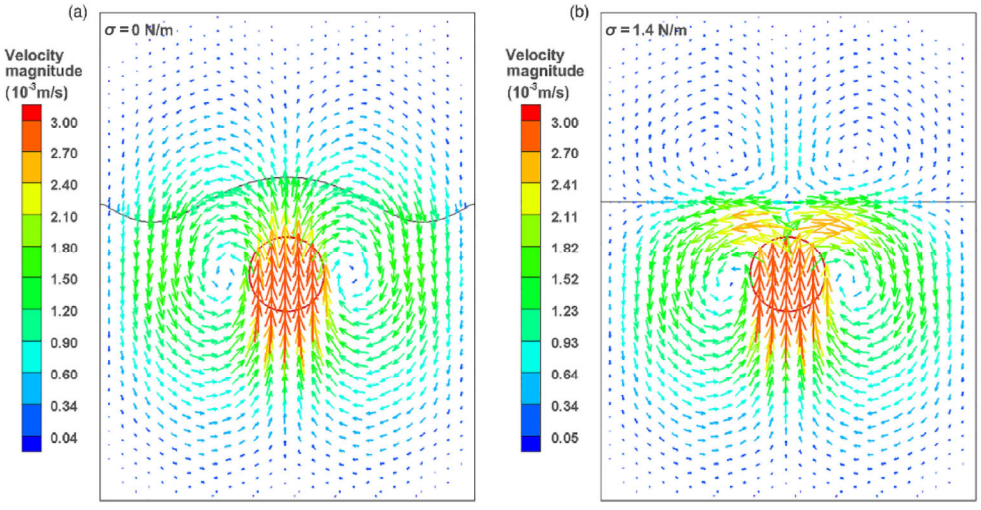

Fig. 4 Velocity vectors in the vicinity of the approaching particle and the steel–slag interface, for the case (a) with no interfacial tension at the interface, and (b) with the realistic condition of σ_{MS} = 1.4 N/m. The steel–slag interface is represented by the solid black line, and the particle location is marked with the red circle.

3 Results

3.1 Grid sensitivity study

To ensure the accuracy of numerical solution, a grid sensitivity analysis based on the reference case (see Table 2) has been performed. Three sizes of grid are built, namely a coarse, medium, and fine grid, with a minimum size of 3, 2.5, and 2 μm, respectively. Due to a particular interest in the vicinity of the three-phase contact area, the grid refinement depends on a continuous increase in the mesh layers around the particle surface (see the component grid shown in Fig. 1(c)). Accordingly, the regular Cartesian grid with a similar grid size to the component is applied to the cuboid fluid region. In the course of a particle separation at the steel–slag interface, the particle's force, velocity, and displacement are three fundamental physical quantities related to particle motion. The evolutions of these three quantities over time under different grids are compared and presented in Fig. 5. Overall, a subtle change can be observed from the medium grid to the fine grid for all three quantities. In contrast, using the coarse grid results in an overestimation of the numerical values. Although the velocity and displacement obtained from the medium and the fine grid show slight differences since 5×10^{-5} s, both grid sizes produce the same results on the equilibrium position of the particle, which is a reference value of whether particle can be entirely removed or not and of particular interest in current simulations. Besides, the medium grid with a size of around 2.5 μm is already able to show a clear and sharp steel–slag interface. Meanwhile, it has superiority in computational time over the fine grid. Thus, the medium grid provides acceptable solutions and is used for the following simulation cases.

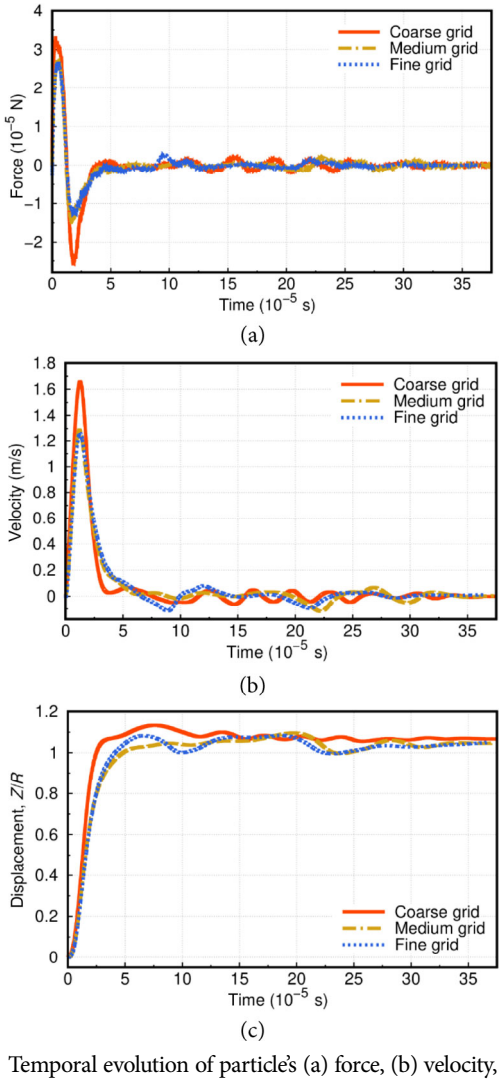

Fig. 5 Temporal evolution of particle's (a) force, (b) velocity, and (c) displacement (made dimensionless with particle radius R, the same for the remaining displacement–time figures) at different grids.

3.2 Particle's dynamic behavior at the steel–slag interface

The interactions of a particle with the steel–slag interface have been modelled for three different conditions. According to the wettability of particle surface with respect to the slag phase, the three conditions refer to (i) particle surface is of higher wettability with the slag, (ii) equal wettability to steel and slag, and (iii) particle surface is of lower wettability with the slag, wherein (i) and (iii) can be described as "slagophilic" and "slagophobic", respectively.

As presented in Fig. 6, for different contact angles, the evolution of interface under the interaction of particles is similar. Specifically, once a particle contacts with the initial flat interface, a concave meniscus forms, and the resulting vertical capillary force acts as a driving force for the moving particle. Then the interface is continuously evolving as the particle moves upwards. At some point, the interface in the vicinity of the three-phase line is almost flat ($t = 2.3 \times 10^{-5}$ s in Fig. 6(a), $t = 2.4 \times 10^{-5}$ s in Fig. 6(b), and $t = 1.4 \times 10^{-5}$ s in Fig. 6(c)). Afterwards, the capillary force reverses direction and tries to slow down the particle ($t = 3.2 \times 10^{-5}$ s, 3.6×10^{-5} s, and 2.4×10^{-5} s in Figs. 6(a), 6(b), and 6(c), respectively).

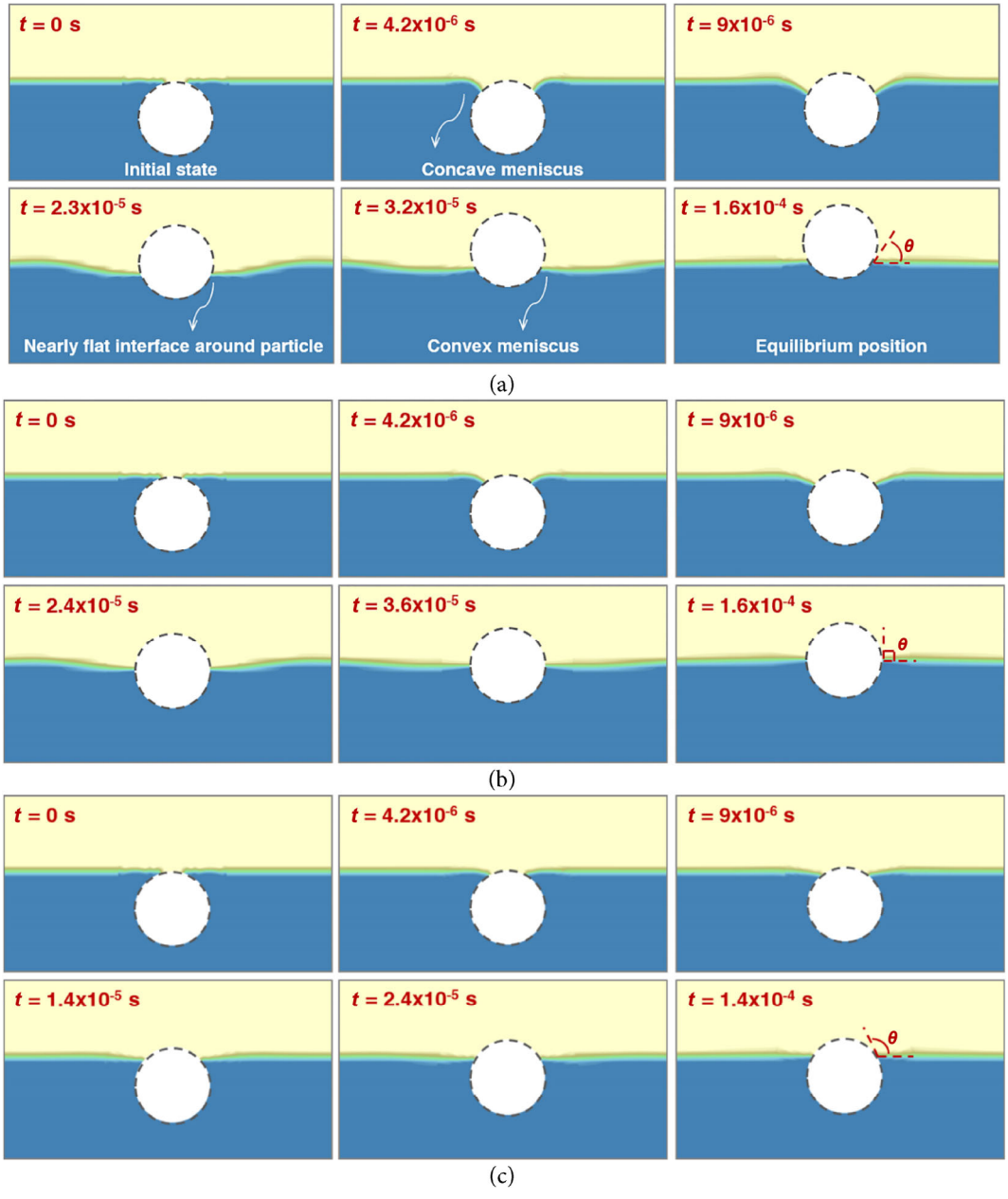

Fig. 6 Evolution of particle motion across the steel–slag interface under different contact angles θ_{IMS}: (a) 60°, (b) 90°, and (c) 120°, which is observed from the $X = 0$ plane. The blue region represents the steel phase; the upper yellow area is the slag layer; the particle is identified by the gray dotted boundary.

For these three cases, particles always stay in an equilibrium position at the interface in the end. In comparison, the three situations mainly differ in varying degrees of interfacial deformation and the transition position of liquid level shapes, i.e., from a concave meniscus to a partially nearly flat interface then to a convex meniscus. These differences affect the capillary force acting on a particle, leading to different motion processes and final equilibrium positions. When the contact angle is 90°, particle stays neutral at the interface. Compared to the slagophobic particle ($\theta_{IMS} > 90°$) which barely contacts with the slag, the slagophilic particle ($\theta_{IMS} < 90°$) shows a larger tendency to enter into the slag phase, but it will still get trapped at the interface. Considering the contact angle of typical inclusions in the steel industry lies above 40°, besides the three cases discussed above, situations with smaller contact angles are further investigated, as shown in Figs. 7 and 8. Under the current simulation conditions, it is found that the particle is completely separated at a contact angle of around 20°.

Figure 9 further compares the temporal evolution of fundamental quantities—particle's (a) force, (b) velocity, and (c) displacement during the separation process under different contact angles. In general, the force acting on a particle has a positive effect on particle motion firstly and then plays a negative role. In both stages, the force increases to a peak value and then decreases, but the positive stage exceeds. Finally, the force goes to zero. It is worth noting that in a very short time at the beginning, the force is negative, causing the particle to move downwards (Fig. 9(b)), which indicates consideration on initial velocity is nonsignificant.

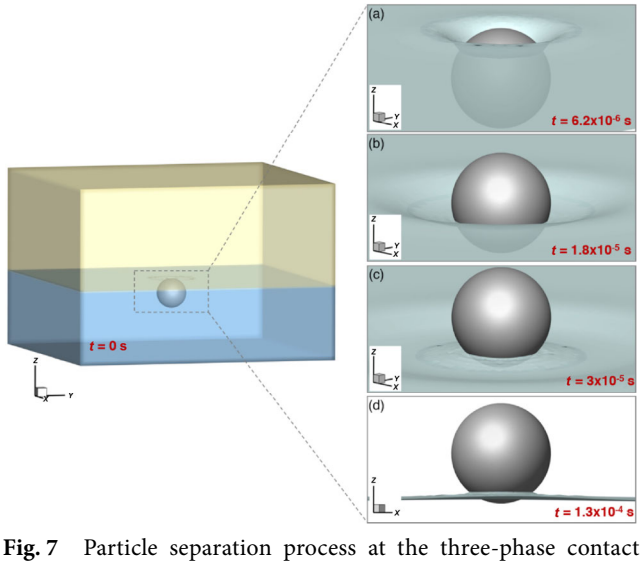

Fig. 7 Particle separation process at the three-phase contact angle of 40°. Snapshot on the left side provides a full view of the initial state in which the particle just contacts with the flat steel–slag interface. Particle motion and the evolution of the surrounding meniscus are shown in closeups (a)–(d) on the right side in chronological order.

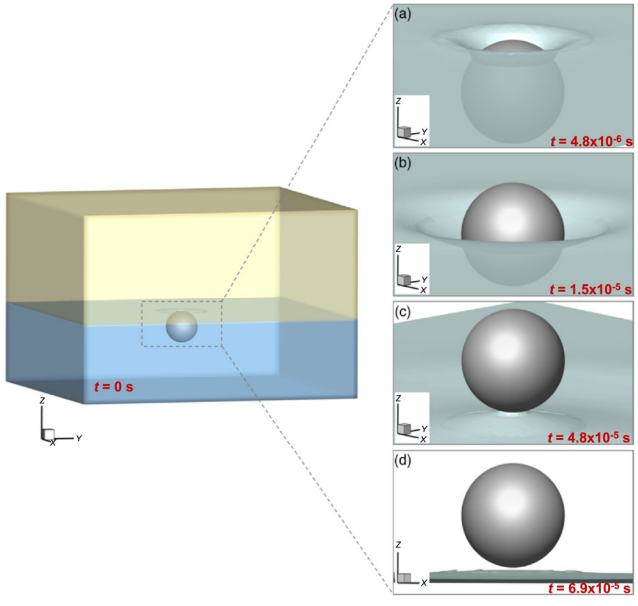

Fig. 8 A complete separation in which the three-phase contact angle is 20°. Snapshot on the left side provides a full view of the initial state in which the particle just contacts with the flat steel–slag interface. Particle motion and the evolution of the surrounding meniscus are shown in closeups (a)–(d) on the right side in chronological order.

The reason for this phenomenon will be discussed in Section 4. According to the force, a particle generally undergoes a faster acceleration stage with the action of positive force, then gradually slows down due to the downward force, and finally enters into slag or remains at an equilibrium position at the interface when its velocity goes zero. Particle moves at a considerable velocity compared to the terminal rising velocity which is only in the order of 10^{-3} m/s for the same size particle (i.e., 50 μm) (Odenthal et al., 2010), demonstrating the significant effect of capillary force for the separation process. The same trends but numerical differences for situations with different contact angles are observed. For the slagophilic particle, its displacement is above one radius, meaning a larger part of the particle is in the slag phase. With the contact angle decreasing, the interfacial curvature is becoming more extensive, resulting in faster acceleration and a slight change for the deceleration stage. Therefore, the smaller the contact angle is, the higher position the particle could arrive. Under current calculation conditions, the particle requires excellent wettability to be removed from the interface completely, which corresponds to a contact angle of around 20°. Compared to the slagophilic case, when the three-phase contact angle is 90°, that is, the steel and slag phases have the same wetting ability to the particle surface, particle finally remains neutral at the interface (one-radius displacement seen from Fig. 9(c)). The bad separation happens if the contact angle is larger than 90°, and only a small part of

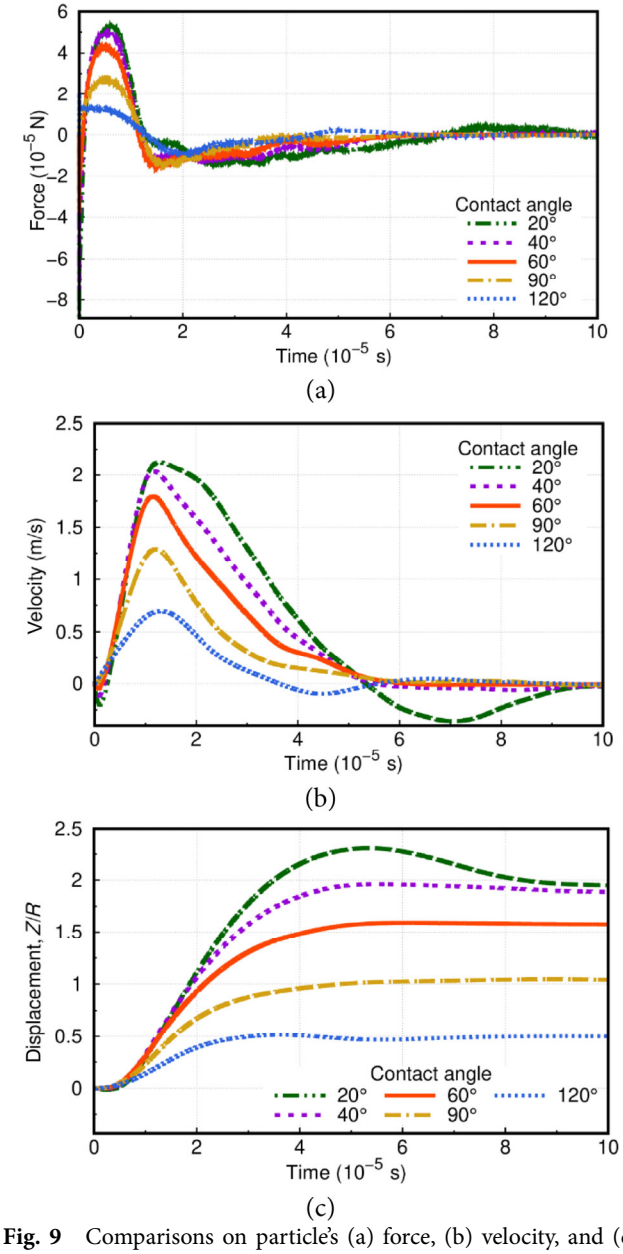

Fig. 9 Comparisons on particle's (a) force, (b) velocity, and (c) displacement during the separation process under different contact angles.

the particle contacts with the slag layer in this case. All of the results also match well with the previous observations from the contour of volume fraction.

3.3 Parameter studies

3.3.1 Interfacial tension of steel–slag interface

As the first parameter, the effect of interfacial tension between steel and slag on the process of particle separation at the interface is investigated. Thus, in addition to the reference case with σ_{MS} = 1.4 N/m, three more cases with σ_{MS} = 0.7, 0.14, and 0 N/m are simulated, as listed in Table 2. The latter corresponds to the condition where no capillary forces act at the interface. Even though this is a non-physical condition, it could help to understand the impact of capillary forces on particle separation at the interface. Figure 10 presents the changes in physical quantities (a) force, (b) velocity, and (c) displacement of a particle under different interfacial tensions. For cases with $\sigma_{MS} \neq 0$, each motion-related quantity has the same varying tendency. In general, the force can change successively in two directions, positive and negative, resulting in increasing and following decreasing in particle velocity. Particle experiences these

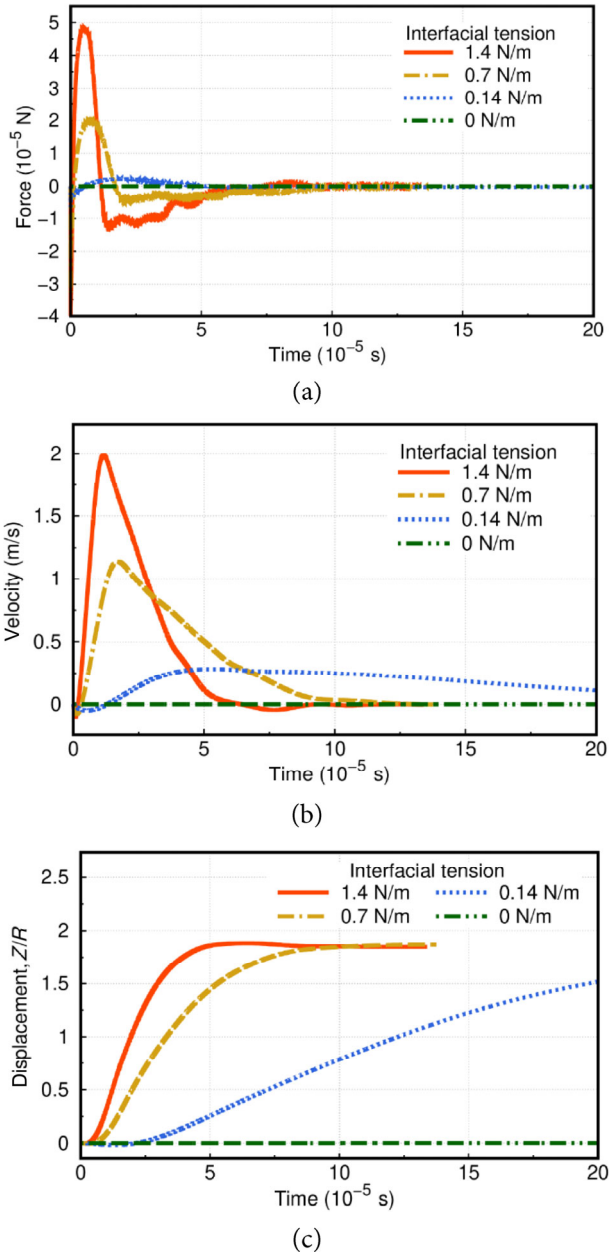

Fig. 10 Effect of interfacial tension on motion characteristics of particle's (a) force, (b) velocity, and (c) displacement at the steel–slag interface.

stages and reaches an equilibrium state at the interface in the end. The difference is that, as can be seen from Fig. 10(a), the higher the interfacial tension is, the larger the maximum force and the faster the force changes are. Then depending on the force, for the case with smaller interfacial tension, the peak value of velocity is smaller, and changes on both the acceleration and deceleration stages are slower than the situation with high interfacial tension. It is observed from Fig. 10(c) that particle eventually takes different amounts of time to get an equilibrium position. For the case with σ_{MS} = 1.4 N/m, it takes 4×10^{-4} s to get this position. The equilibrium positions vary from 1.81*R* to 1.87*R* depending on the interfacial tension, which generally shows little change compared to the result by changing contact angle. Obviously, without considering interfacial tension, the force acting on a particle is much smaller (only in the order of 10^{-9} N), and the particle hardly moves compared to the other three cases. The results indicate that the gravitational effect is nonsignificant compared to the capillary action during the process of a micro-sized particle motion at the steel–slag interface. Moreover, a higher interfacial tension could speed up the separation process but has less effect on the particle's equilibrium position. However, in practice, the interfacial tensions affect the contact angle rather than being treated as a fixed value, which requires a comprehensive consideration in future study.

3.3.2 *Particle diameter*

The size of inclusions in molten steel usually ranges from 1 μm below to more than 100 μm based on different sources. It is well known that particle size largely influences its drifting behavior, as for its influence on the interfacial separation process is of interest here. Therefore, besides the reference case (50 μm in diameter), a larger particle (100 μm) and a smaller particle (25 μm) are included to investigate how particle size affects its motion at the interface. Figure 11 shows changes in motion-related quantities for a particle with different diameters. The same changing trends, as described in Sections 3.2 and 3.3.1, are observed. Thus, particle shares similar motion characteristics, as mentioned before. It can be seen from Fig. 11(a), doubling the particle diameter results in approximately doubling in the peak value of the force, which is mainly due to the increment in the three-phase contact area and the resulting capillary force. However, the larger the particle diameter is, the slower the speed changes, corresponding to Fig. 11(b). The reason should be the change in particle volume caused by the change in its diameter is much more than the force, especially for a sphere, leading to a smaller acceleration. It is found that particle's equilibrium position changes within the range from 1.78*R* to 1.85*R*, which is less affected by particle diameter. However, different particle sizes evidently

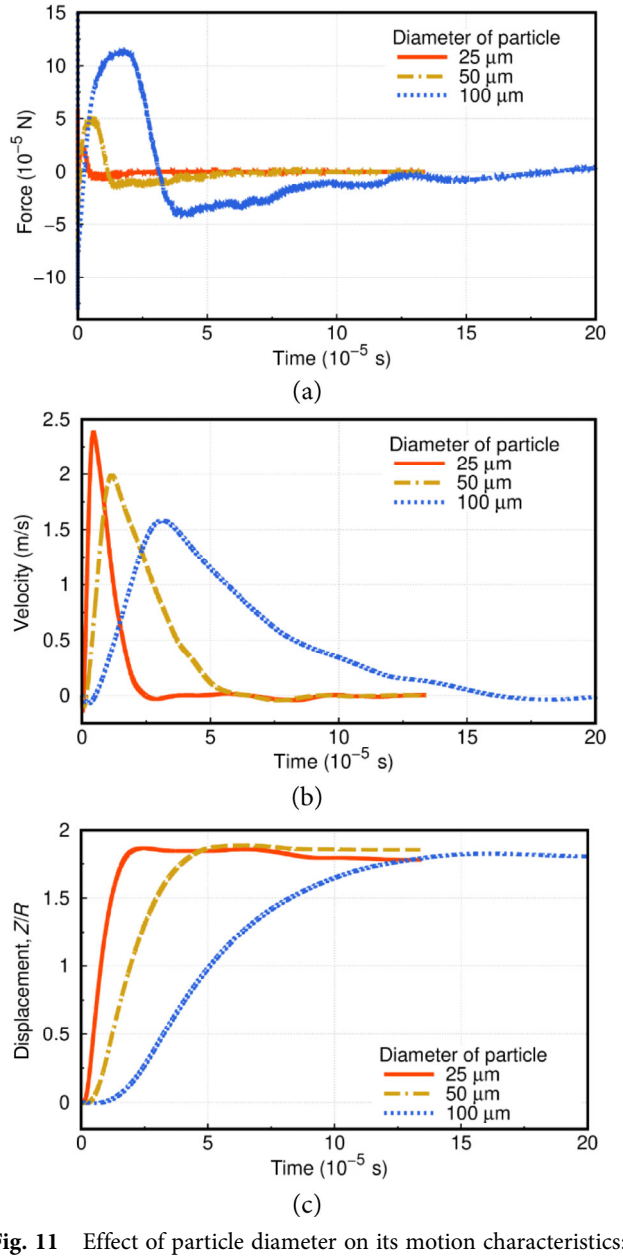

Fig. 11 Effect of particle diameter on its motion characteristics: (a) force, (b) velocity, and (c) displacement at the steel–slag interface.

affect the time required to reach an equilibrium position, and the larger the particle is, the longer time is required. It seems to be a conflict with the drifting stage, where a larger particle is easier to arrive at the interface. However, it should be noticed that a large ratio of surface area to volume is important for interfacial separation in which the capillary force dominates.

3.3.3 *Particle density*

Moreover, the influence of particle density on its motion behavior at the steel–slag interface is investigated. As the reference case is shown in Table 2, the most common inclusions have a higher density than metallurgical slags.

Nonetheless, two more cases that the particle is of equal density with the slag phase or lighter than it are considered. This could demonstrate the effect of buoyancy force on interfacial separation as well. According to Fig. 12, almost consistent changing trends for each quantity are observed, which indicates that particle density only has a minor influence. It is clear that if a particle is fully immersed in the steel phase, its motion will be decided by the net force which arises from the density differences between the fluid and the particle and increases with the decreasing particle density. Thus, the current results reflect again that the gravitational effect is much less than the capillary effect for particle separation at the steel–slag interface.

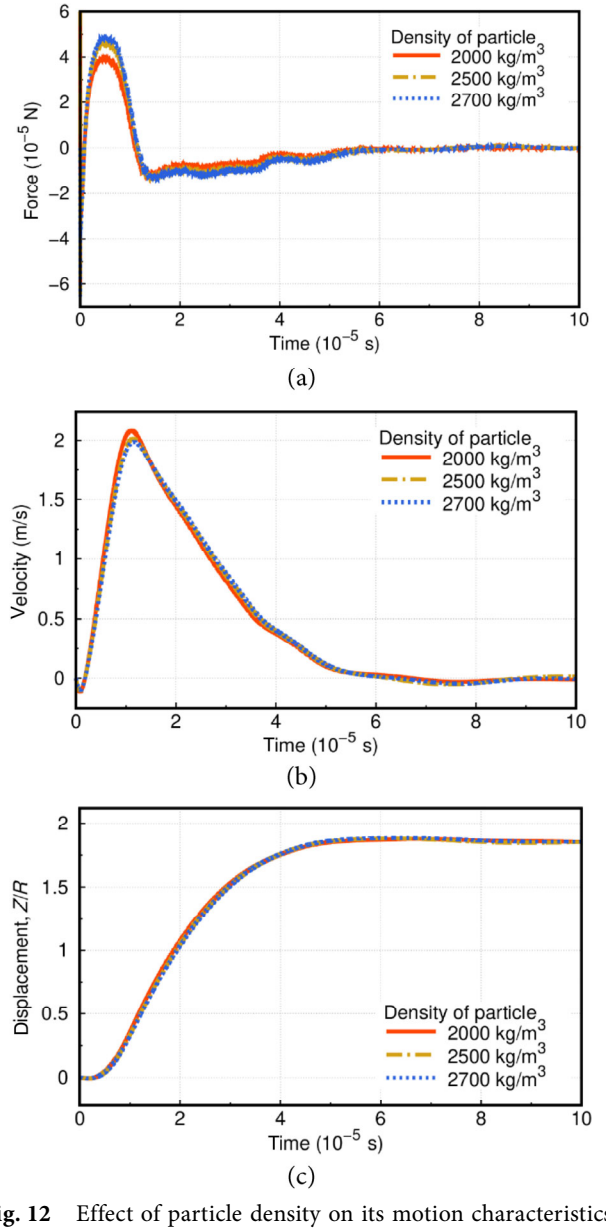

Fig. 12 Effect of particle density on its motion characteristics: (a) force, (b) velocity, and (c) displacement at the steel–slag interface.

4 Discussion

The parameter study in Section 3.3 indicates the significant role of capillary forces in particle interfacial separation. This point is also mentioned in the existing studies (Shannon and Sridhar, 2005; Costa e Silva, 2018). Generally, the Bond number $Bo = (\rho_M - \rho_S)R_I^2 g/\sigma_{MS}$ is used to quantify the scale of gravitational effect and capillary effect (Bresme, 2018; Ballard et al., 2019), which is smaller than 10^{-4} for the general steel–slag–particle system. It means the interfacial capillary interaction dominates for a micro-sized particle at the steel–slag interface. The capillary forces arise from interfacial deformation, which is in essence a corollary of the dynamic balance among interfacial tensions. However, the existing mathematical models generally leave the meniscus out of consideration, leading to a less accurate estimation of the capillary forces and particle's dynamic motion (Nakajima and Okamura, 1992; Strandh et al., 2005a; Liu et al., 2016). In comparison, the current numerical model is able to show the dynamic interactions between a spherical particle and the steel–slag interface, including the formation and evolution of meniscus under particle action and particle motion under the resulting capillary force. Besides, current simulations reveal two phenomena that are also closely related to interfacial properties and hard to be depicted by existing models. Figure 13 shows once a particle touches the interface, it will decelerate and be pushed away slightly from the interface instead of moving upwards immediately, as the three-phase system tries to establish an equilibrium state in that instant at a given contact angle. This causes a quite high velocity compared to particle's terminal velocity, and the effect is stronger for the smaller contact angle. Therefore, it demonstrates the rationality of the initial assumption about starting simulations with zero initial velocity. Secondly, existing studies usually assume that a particle is fully separated to the slag if the particle center has traveled one-particle-diameter distance (Nakajima and Okamura, 1992). However, it is not a good criterion to determine a complete separation. Figure 14 shows the steel–slag–particle system at $t = 3.7 \times 10^{-5}$ s under the contact angle of 20°. Although the particle is already above the original liquid level, its motion is still affected by a convex meniscus that tries to pull the particle back. The lack of consideration of the meniscus's effect might estimate the critical contact angle inaccurately.

According to the present results, a complete separation for the spherical inclusion occurs when θ_{IMS} is about 20°. The contact angle is smaller than that of common inclusions, such as alumina, varying approximately in the range of 39°–53° due to differences in slag composition (Nakajima and Okamura, 1992; Xuan et al., 2019). The simulation results

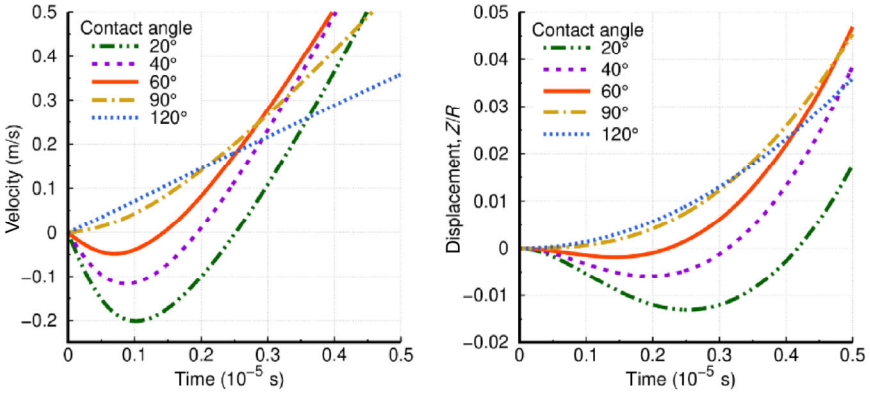

Fig. 13 Particle's velocity and displacement variations at the very beginning of the separation under different contact angles.

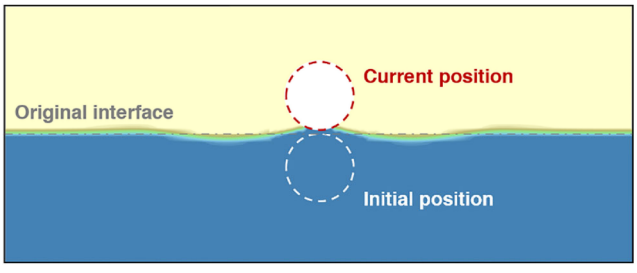

Fig. 14 Relative position of a particle and the steel–slag interface at $t = 3.7 \times 10^{-5}$ s under the contact angle of 20°.

may draw a conclusion that is contradictory to the usual assumption that inclusions are removed once they arrive at the interface by the steel flow. However, the experimental studies related to the behavior of inclusions at the steel–slag interface also suggest that a limited separation may exist in industrial vessels. Inclusions at a slag–metal interface were observed in situ with a confocal scanning laser microscope (CSLM) (Mu et al., 2018). This approach enables the visualization of the steel–slag interface and inclusions at steelmaking temperatures as the liquid slag is optically transparent. It was reported that most inclusions (including alumina or alumina-rich inclusions) observed during experiments remained at the slag side of the interface. Their stay led to agglomeration of solid inclusions or liquid inclusions capturing solid ones at the interface, and inclusions re-entrained into the metal were observed in a few cases (Misra et al., 2000; Lee et al., 2001; Coletti et al., 2003; Vantilt et al., 2004). Misra et al. (2000) also found that only small spherical Ca–Al–O type liquid inclusions with a diameter less than 10 μm were fully separated into the $CaO–Al_2O_3$ slag. However, a significant rest time (3–4 s) was needed at the interface. This time is much longer than the separation stage dominated by the capillary effect based on current simulations, indicating other factors may govern the removal process together. In general, both the numerical and the experimental studies indicate that the rest time for inclusions at the steel–slag interface may be quite long in reality. On top of that, at least three remaining questions need to be further investigated: (1) how a faster separation can be achieved by tailoring the inclusions. Specifically, a study on influential factors related to the wetting behavior of particles such as surface texture (roughness and particle morphology), surface chemistry, and hydrodynamic conditions (Good, 1992; Mukai, 2005; Chau et al., 2009) could be an important topic; (2) if a Marangoni-induced flow by particle dissolution further enhances particle separation (Orino et al., 1984; Mukai, 2005; Park et al., 2009); (3) what the critical condition of re-entrainment is for inclusions not separated enough. The interfacial turbulence might be responsible for this (Cleaver and Yates, 1973). These aspects will be the focus of future studies, which are believed to be feasible based on the current numerical method and beneficial to separation process optimization.

5 Conclusions

The dynamics of a spherical particle interacting with the steel–slag interface is numerically investigated using the volume of fluid method in combination with the overset grid technique to account for particle motion. A sensitivity analysis on the effect of different physical parameters in the steel–slag–particle system is also carried out. The main findings are summarized as follows:

(1) The described model is able to capture the formation and continuous evolution of a meniscus accompanying the dynamic interactions of a micro-sized particle with the steel–slag interface. For a spherical particle, a meniscus transforming from an originally established concave shape to a convex one exerts both positive and negative effects, and the resulting capillary force from interfacial deformation shows a major contribution to particle motion. Accordingly, the particle generally accelerates first to a quite high velocity (about three orders of magnitude larger than its terminal velocity), then undergoes a deceleration stage and is trapped at the interface or separated to the slag in the end.

(2) The wettability of particle with the slag phase is the main factor affecting the separation behavior (trapped at the interface or fully separated into slag). Particles with a small three-phase contact angle are more likely to enter the slag phase. A complete separation for a spherical particle is achieved at the contact angle of about 20° under current simulation conditions, while particles with a larger contact angle tend to stay at an equilibrium position at the interface.

(3) For particles staying at the interface, the other parameters make a slight difference in the equilibrium position, but they have a great effect on particle motion, especially for different interfacial tensions and particle diameters. Higher interfacial tension of fluid interface and smaller size of particle speed up the motion process. In comparison, particle density basically does not make a difference when the motion is dominated by the capillary effect.

Future work will focus on the factors that could further influence particle separation behavior at the steel–slag interface. The priorities are (i) the solutal Marangoni effect induced by particle dissolution and (ii) the wetting behavior influenced by particle roughness and morphology. These studies are expected to be feasible based on the model presented here.

Acknowledgements

The authors gratefully acknowledge the funding support of K1-MET GmbH, a metallurgical competence center. The research program of the K1-MET competence center is supported by COMET (Competence Center for Excellent Technologies), the Austrian program for competence centers. COMET is funded by the Federal Ministry for Climate Action, Environment, Energy, Mobility, Innovation and Technology, the Federal Ministry for Digital and Economic Affairs, the Federal States of Upper Austria, Tyrol and Styria, as well as the Styrian Business Promotion Agency (SFG). In addition to the public funding from COMET, this research project is partially financed by the industrial partners (voestalpine Stahl Linz GmbH, voestalpine Stahl Donawitz GmbH, and RHI Magnesita GmbH).

Funding note

Open access funding provided by Johannes Kepler University Linz.

Declaration of competing interest

The authors have no competing interests to declare that are relevant to the content of this article.

References

Aveyard, R., Clint, J. H., Nees, D. 2000. Small solid particles and liquid lenses at fluid/fluid interfaces. *Colloid Polym Sci,* 278: 155–163.

Ballard, N., Law, A. D., Bon, S. A. F. 2019. Colloidal particles at fluid interfaces: Behaviour of isolated particles. *Soft Matter*, 15: 1186–1199.

Bouris, D., Bergeles, G. 1998. Investigation of inclusion re-entrainment from the steel–slag interface. *Metall Mater Trans B*, 29: 641–649.

Brackbill, J. U., Kothe, D. B., Zemach, C. 1992. A continuum method for modeling surface tension. *J Comput Phys,* 100: 335–354.

Bresme, F. 2018. Theoretical approaches to investigate anisotropic particles at fluid interfaces. In: *Anisotropic Particle Assemblies*. Wu, N., Lee, D., Striolo, A., Eds. Amsterdam: Elsevier, 233–260.

Chau, T. T., Bruckard, W. J., Koh, P. T. L., Nguyen, A. V. 2009. A review of factors that affect contact angle and implications for flotation practice. *Adv Colloid Interface Sci*, 150: 106–115.

Choi, J. Y., Lee, H. G. 2003. Wetting of solid Al_2O_3 with molten $CaO–Al_2O_3–SiO_2$. *ISIJ Int*, 43: 1348–1355.

Cleaver, J. W., Yates, B. 1973. Mechanism of detachment of colloidal particles from a flat substrate in a turbulent flow. *J Colloid Interface Sci*, 44: 464–474.

Coletti, B., Blanpain, B., Vantilt, S., Sridhar, S. 2003. Observation of calcium aluminate inclusions at interfaces between Ca-treated, Al-killed steels and slags. *Metall Mater Trans B*, 34: 533–538.

Coletti, B., Blanpain, B., Vantilt, S., Sridhar, S. 2003. Observation of calcium aluminate inclusions at interfaces between Ca-treated, Al-killed steels and slags. *Metall Mater Trans B*, 34: 533–538.

Costa e Silva, A. 2018. Non-metallic inclusions in steels–origin and control. *J Mater Res Technol*, 7: 283–299.

Good, R. J. 1992. Contact angle, wetting, and adhesion: A critical review. *J Adhes Sci Technol*, 6: 1269–1302.

Hirt, C. W., Nichols, B. D. 1981. Volume of fluid (VOF) method for the dynamics of free boundaries. *J Comput Phys*, 39: 201–225.

Lee, S. H., Tse, C., Yi, K. W., Misra, P., Chevrier, V., Orrling, C., Sridhar, S., Cramb, A. W. 2001. Separation and dissolution of Al_2O_3 inclusions at slag/metal interfaces. *J Non-Cryst Solids*, 282: 41–48.

Lin, P. 2007. A fixed-grid model for simulation of a moving body in free surface flows. *Comput Fluids*, 36: 549–561.

Liu, C., Yang, S., Li, J., Zhu, L., Li, X. 2016. Motion behavior of nonmetallic inclusions at the interface of steel and slag. Part I: Model development, validation, and preliminary analysis. *Metall Mater Trans B*, 47: 1882–1892.

Michelic, S., Goriupp, J., Feichtinger, S., Kang, Y. B., Bernhard, C., Schenk, J. 2016. Study on oxide inclusion dissolution in secondary steelmaking slags using high temperature confocal scanning laser microscopy. *Steel Res Int*, 87: 57–67.

Miki, Y., Thomas, B. G. 1999. Modeling of inclusion removal in a tundish. *Metall Mater Trans B*, 30: 639–654.

Misra, P., Chevrier, V., Sridhar, S., Cramb, A. W. 2000. *In situ* observations of inclusions at the (Mn,Si)-killed steel/$CaO–Al_2O_3$ interface. *Metall Mater Trans B*, 31: 1135–1139.

Mu, W., Dogan, N., Coley, K. S. 2018. *In situ* observations of agglomeration of non-metallic inclusions at steel/Ar and steel/slag interfaces by high-temperature confocal laser scanning microscope: A review. *JOM*, 70: 1199–1209.

Mukai, K. 2005. Interfacial phenomena, metals processing and properties. In: *Fundamentals of Metallurgy*. Seetharaman, S., Ed. Sawston: Woodhead Publishing, 237.

Nakajima, K., Okamura, K. 1992. Inclusion transfer behavior across molten steel–slag interface. In: Proceedings of the 4th International Conference on Molten Slags and Fluxes, Tokyo, Japan, 505.

Odenthal, H. J., Javurek, M., Kirschen, M., Vogl, N. 2010. CFD benchmark for a single strand tundish (Part II). *Steel Res Int*, 81: 529–541.

Orino, K., Hara, S., Miwa, T., Kimoto, S. 1984. The effect of oxygen content in molten iron on the interfacial tension between molten iron and slag. *Trans Iron Steel Inst Jpn*, 24: 522–531.

Park, J. H., Jung, I. H., Lee, H. G. 2006. Dissolution behavior of Al_2O_3 and MgO inclusions in the CaO–Al_2O_3–SiO_2 slags: Formation of ring-like structure of $MgAl_2O_4$ and Ca_2SiO_4 around MgO inclusions. *ISIJ Int*, 46: 1626–1634.

Park, S. C., Gaye, H., Lee, H. G. 2009. Interfacial tension between molten iron and CaO–SiO_2–MgO–Al_2O_3–FeO slag system. *Ironmak Steelmak*, 36: 3–11.

Reis, B. H., Bielefeldt, W. V., Vilela, A. C. F. 2014. Efficiency of inclusion absorption by slags during secondary refining of steel. *ISIJ Int*, 54: 1584–1591.

Schellenberger, F., Papadopoulos, P., Kappl, M., Weber, S. A. L., Vollmer, D., Butt, H. J. 2018. Detaching microparticles from a liquid surface. *Phys Rev Lett*, 121: 048002.

Shannon, G. N., Sridhar, S. 2005. Film-drainage, separation and dissolution of Al_2O_3 inclusions across interfaces between molten steel and ladle-, tundish- and mold-slags. *High Temp Mater Process*, 24: 111–124.

Shannon, G., White, L., Sridhar, S. 2008. Modeling inclusion approach to the steel/slag interface. *Mater Sci Eng A*, 495: 310–315.

Snyder, D., Koutsavdis, E., Anttonen, J. 2003. Transonic store separation using unstructured CFD with dynamic meshing. In: Proceedings of the 33rd AIAA Fluid Dynamics Conference and Exhibit, Washington DC, 3919.

Sridhar, S., Cramb, A. W. 2000. Kinetics of Al_2O_3 dissolution in CaO–MgO–SiO_2–Al_2O_3 slags: In situ observations and analysis. *Metall Mater Trans B*, 31: 406–410.

Strandh, J., Nakajima, K., Eriksson, R., Jönsson, P. 2005a. Solid inclusion transfer at a steel–slag interface with focus on tundish conditions. *ISIJ Int*, 45: 1597–1606.

Strandh, J., Nakajima, K., Eriksson, R., Jönsson, P. 2005b. A mathematical model to study liquid inclusion behavior at the steel–slag interface. *ISIJ Int*, 45:1838–1847.

Tang, Y., Cheng, S. 2018. Capillary forces on a small particle at a liquid-vapor interface: Theory and simulation. *Phys Rev E*, 98: 032802.

Thomas, B. G., Zhang, L. 2001. Mathematical modeling of fluid flow in continuous casting. *ISIJ Int*, 41: 1181–1193.

Vantilt, S., Coletti, B., Blanpain, B., Fransaer, J., Wollants, P., Sridhar, S. 2004. Observation of inclusions in manganese-silicon killed steels at steel–gas and steel–slag interfaces. *ISIJ Int*, 44: 1–10.

Xuan, C., Persson, E. S., Sevastopolev, R., Nzotta, M. 2019. Motion and detachment behaviors of liquid inclusion at molten steel–slag interfaces. *Metall Mater Trans B*, 50: 1957–1973.

Zhang, L., Taniguchi, S., Cai, K. 2000. Fluid flow and inclusion removal in continuous casting tundish. *Metall Mater Trans B*, 31: 253–266.

Zhang, L., Thomas, B. G. 2003. State of the art in evaluation and control of steel cleanliness. *ISIJ Int*, 43: 271–291.